Journal of Geodynamics 94–95 (2016) 68–83

Contents lists available at ScienceDirect

Journal of Geodynamics

journal homepage: http://www.elsevier.com/locate/jog

Review

Tectonic inversion and magmatism in the Lautaro Basin, northern Chile, Central Andes: A comparative approach from field data and analog models

Fernando Martínez [a,*], Marco Bonini [b], Domenico Montanari [b], Giacomo Corti [b]

[a] Department of Geology, FCFM, University of Chile, Santiago de Chile, Plaza Ercilla 803, Chile
[b] Instituto di Geoscienze e Georisorse, Consiglio Nazionale delle Ricerche, Via G. La Pira, Florence 50121, Italy

ARTICLE INFO

Article history:
Received 1 September 2015
Received in revised form 18 January 2016
Accepted 5 February 2016
Available online 16 February 2016

Keywords:
Tectonic inversion
Magmatism
Lautaro Basin
Inverted faults
Inversion anticlines

ABSTRACT

We present the results of a series of analog models addressing the relationships between tectonic inversion and magmatism, taking the Lautaro Basin in northern Chile (27–28° S), Central Andes as a natural case. The experiments consisted of extension and orthogonal shortening of sand–silicone models to reproduce the tectonic inversion of a previous extensional system synchronous with the emplacement of analog magma. We analyzed how the variation in the rate of magma intrusion, shortening, and syn-compressive sedimentation may affect the final configuration of an inverted system, and the results were compared with field observations. Our results showed that (i) folding of syn-rift deposits and increased steepness of the master faults accommodate the shortening of the extensional system, (ii) magmatic intrusions condition the final geometries (top view and cross-section) of inverted normal faults in the models and in the Lautaro Basin, (iii) magma tends to migrate preferentially along the inverted faults, and accumulates beneath the faults and in the core of the inversion anticlines, (iv) the syn-inversion magmatism may indicate the migration pathways, which favor major lubrication and slip on the structures during their reactivation.

© 2016 Elsevier Ltd. All rights reserved.

Contents

* Corresponding author.
E-mail address: martinezfjh@hotmail.com (F. Martínez).

http://dx.doi.org/10.1016/j.jog.2016.02.003
0264-3707/© 2016 Elsevier Ltd. All rights reserved.

1. Introduction

Crustal shortening and magmatism are two fundamental geological processes that occur in those orogenic belts established over subduction zones (Barton, 1990; Ernst, 1992; DeCelles et al., 2009). The Central Andes of South America comprise a typical orogenic belt that has resulted from both processes, which have been responsible for their structural configuration (e.g., Mpodozis and Ramos, 1989; Allmendinger et al., 1997; Ramos, 2009). Geological evidences of contemporaneous shortening and magmatism are commonly associated with the coeval occurrence of large thrust systems, volcanic arcs, and plutonic complexes. Previous geological investigations along different regions of the Central Andes have provided descriptions of volcanoes and intrusive bodies in close proximity to thrust faults and folds with different structural relationships, as illustrated in Fig. 1 (Kozlowsky et al., 1996; Godoy et al., 1999; Clavero et al., 2004; Tibaldi, 2005; Galland et al., 2007).

The interplay between compressive deformation and magmatism has been a topic of debate for many years, especially in terms of understand the mechanisms of magma emplacement during the growth of thrust faults and folds, because volcanism and magmatic intrusions were believed to occur only in extensional settings, considering that the tensional stress favors magma upwelling along vertical fractures perpendicular to the least principal stress ($\sigma 3$) direction (Anderson, 1951; Watanabe et al., 1999; Tibaldi et al., 2010); today, however, magma emplacement in compressional settings is mostly accepted because natural examples have been found worldwide (e.g., Tibaldi, 2005, 2008; Galland et al., 2007; González et al., 2009; Montanari et al., 2010). Furthermore, analog modeling of magma emplacement in different compression styles have allowed to understand the natural geometries and relationships that can occur between thrust fault systems and intrusions (Benn et al., 1998, 2000; Galland et al., 2009; Montanari et al., 2010; Ferré et al., 2012).

Good examples of the interactions between compressive structures and intrusions are exhibited in the western slope of the Central Andes in northern Chile. In this region large and kilometric intrusions are exposed along the core of thin and thick-skinned compressive folds (e.g., fault-bend folds, fault-propagation folds, inversion anticlines, among others) as well as along the trace of thrusts and inverted faults (Moscoso and Mpodozis, 1988; Arévalo, 2005; Charrier et al., 2009; Ramos, 2009; Peña et al., 2013). Chronological data and field observations documented from some regions in northern Chile (e.g., Domeyko Cordillera, Lautaro Basin, and Tarapacá Basin) suggest that the compressional deformation and magma emplacement events took place simultaneously during the shortening and tectonic inversion of former Mesozoic extensional basins (e.g., Amilibia and Skarmeta, 2003; Arévalo, 2005; Amilibia et al., 2008; Martínez et al., 2012; Peña et al., 2013).

In these regions some geological questions related to the structural styles, shortening magnitudes, geometry of the basins, ages of stratigraphic units and intrusive bodies have been resolved by geological mapping, structural and chronological techniques, however, some factors such as: (a) the geometric relationship between magmatic intrusions and inverted structures and thrust fault systems in the subsurface (b) the main pathways of magma migration during the tectonic inversion of former extensional basins, (c) the influence the magma migration during the basin inversion and the influence of inherent and new structures formed during episodes of shortening and magmatism are still poorly understood or unresolved. The main reason of this problem is due to the lack of subsurface information, such as, seismic profiles, well deeps or 3D gravity surveys, which help to understand the structural configuration of the subsurface.

In attempting to give new insights to help answer these questions, we analyzed the interplay between the inverted faults, thrust faults, and intrusive bodies, exposed along the Lautaro Basin in northern Chile. The Lautaro Basin is located along the Central Andes flat-slab subduction segment (27–28° S) (Fig. 2) and corresponds to

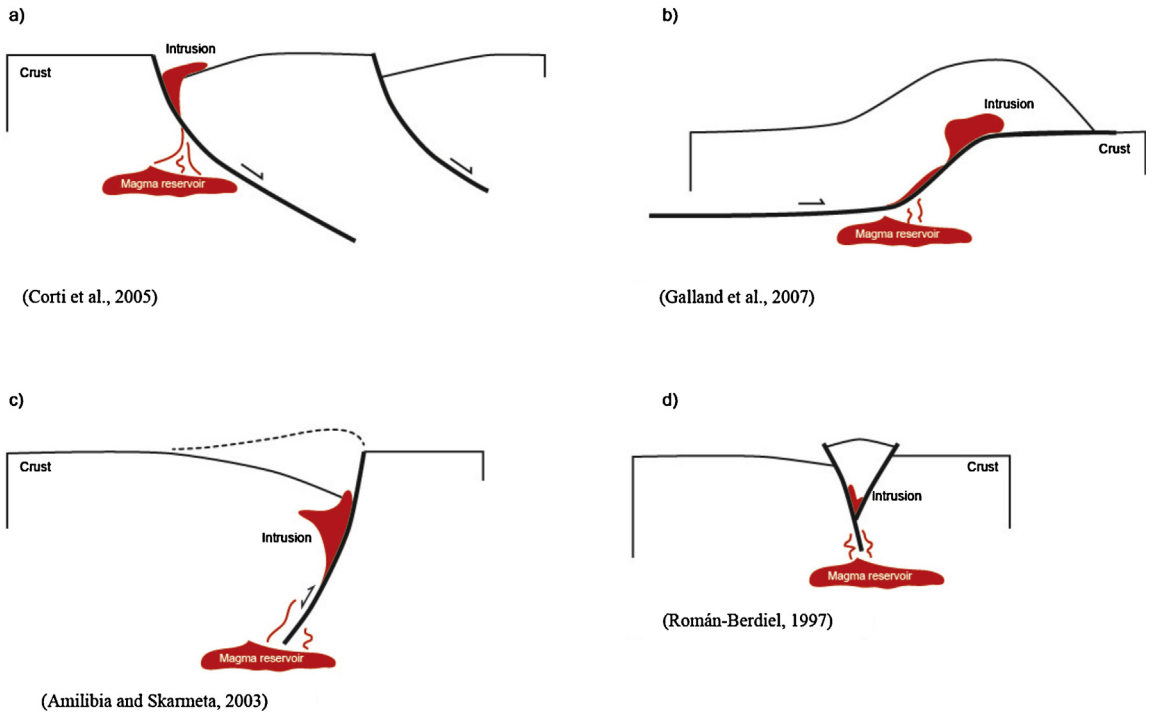

Fig. 1. Schematic models illustrating different modes of magma emplacement along: (a) normal fault systems, (b) purely compressive system dominated by a flat–ramp–flat geometry, (c) partially inverted fault, and (d) strike-slip fault.

Source: Modified from Román-Berdiel (1999), Corti et al. (2005), Amilibia and Skarmeta (2003) and Galland et al. (2007).

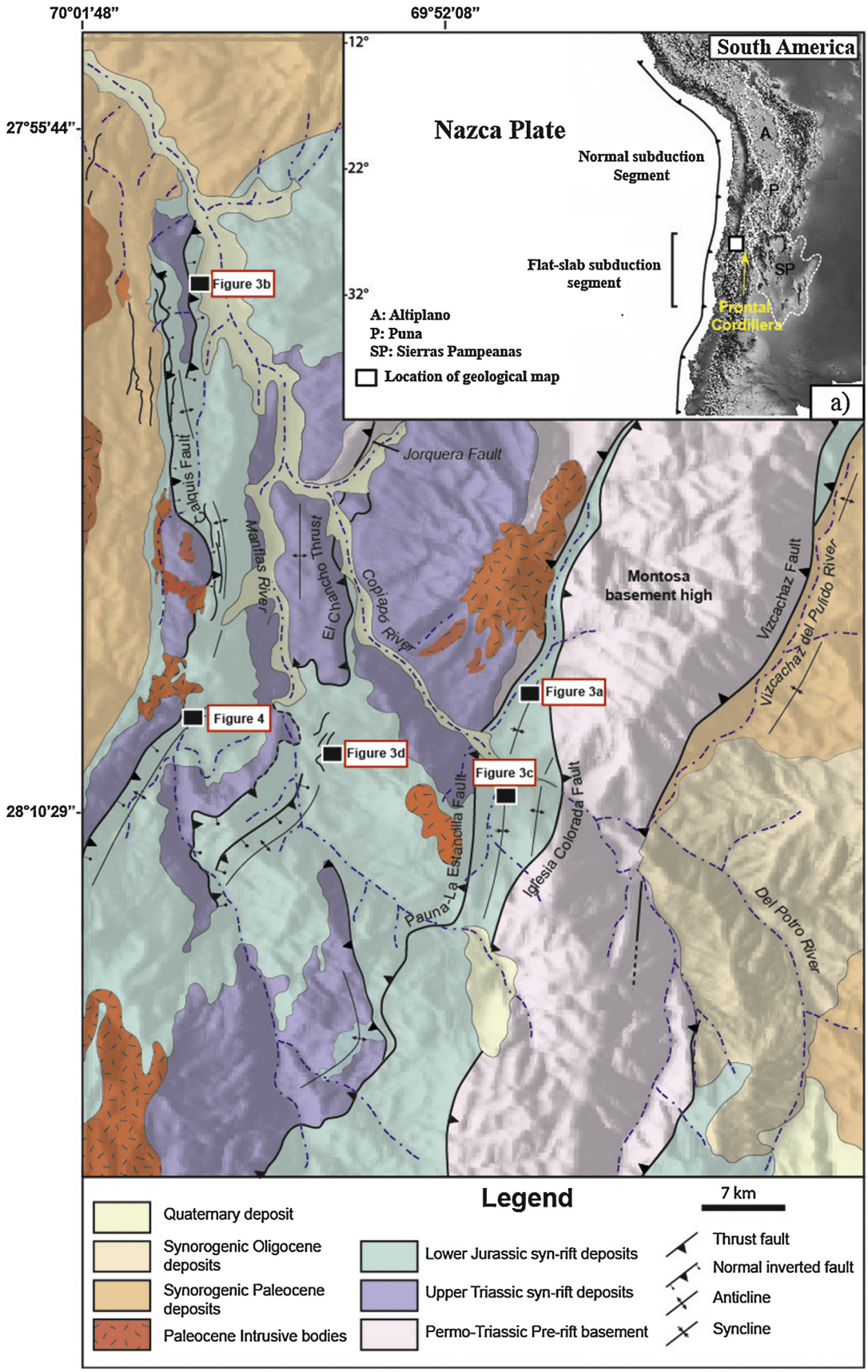

Fig. 2. (a) Location of Lautaro Basin in Central Andes, and (b) simplified geological map of Lautaro Basin in northern Chile, illustrating the distribution of both main geological units and tectonic features.

Source: Modified from Martínez et al. (2012).

a Jurassic half-graben partially inverted during the Cenozoic times (Paleocene–Eocene) (Martínez et al., 2012). Its structure shows as different intrusions (1.5–2 km in length) lie exposed along the master inverted fault, inversion anticlines as well as in the hanging wall of secondary thrust faults (Jensen, 1976; Arévalo, 2005; Martínez et al., 2012; Peña et al., 2013; Fig. 2), which makes this area a ideal place to understand the geometric relationship between magmatic intrusions and inverted structures and thrust fault systems. Considering the absence of subsurface information, we used analog modeling because is a powerful tool to understand the physics of complex tectonic settings as those dominated by tectonic inversion and magmatism. We have used analog models to analyze the process of emplacement of high-viscosity magma during orthogonal shortening and inversion of previous half-grabens, focusing on how the variation in the rate of magma intrusion, shortening, and also how high syn-compressive sedimentation affect their final configuration, and how they compare with the Lautaro Basin.

1.1. Lautaro Basin

The Lautaro Basin is an inverted half-graben, approximately 40 km long and 17 km wide, which trends N–NE and forms part of the western flank of the Chilean Frontal Cordillera (Fig. 2). This basin resulted from a long-lived extensional process that started in the Upper Triassic–Lower Jurassic and could have spread until the Early Cretaceous, such as has been recognized in neighboring areas in Chile (e.g., Chañarcillo and Lagunillas basins) and Argentina (e.g., Salta Basin). The Mesozoic extensional and sag episodes in this region are associated with the stretching and mechanical and thermal subsidence of the western section of the continental margin during the Gondwana break-up (Mpodozis and Ramos, 1989; Mpodozis and Kay, 1990; Aguirre-Urreta, 1993; Mpodozis and Ramos, 2008; Ramos, 2009). Following of these extensional and sag episodes, a major compressional episode occurred along the continental margin during the Late Cretaceous, which was followed by compressives pulses during the Paleocene, and Eocene–Oligocene times (e.g., Peruvian, KT (an episode of Andean deformation (60–65 Ma)), and Incaic events; Cornejo et al., 1993; Maksaev and Zentilli, 1999; Mpodozis et al., 2005; Arriagada et al., 2006; Amilibia et al., 2008), which lead to the shortening and tectonic inversion of the Mesozoic extensional systems (Jensen, 1976; Arévalo, 2005; Martínez et al., 2012; Peña et al., 2013).

The oldest stratigraphic record begins with the pre-rift basement rocks, which are represented by a series of Permo-Triassic basement units, the most important being the "Montosa basement high" (Godoy and Davidson, 1976; Jensen, 1976; Mpodozis and Kay, 1990; Fig. 2). These units are mainly composed of granodiorites, granites, and tonalities, which are well-exposed along the valley of the Copiapó River, and deformed in a thick-skinned style by high-angle, east- and west-dipping reverse faults (Jensen, 1976; Martínez et al., 2012, 2015; Fig. 2). Along this sector, the pre-rift basement is unconformably overlain by ~2100 m of upper-Triassic syn-rift successions made of conglomerates, andesites, and lavas (Fig. 2). To the west of the Montosa basement high (Fig. 2), these successions are unconformably covered by nearly 3000 m of early Jurassic (Sinemurian–Bajocian) marine and continental syn-rift successions that include limestones, calcareous sandstones, and shales with some marine fauna (Jensen, 1976; Arévalo et al., 1994; Arévalo, 2005; Martínez et al., 2012, 2015; Fig. 2). One of the most striking features of the Triassic and Jurassic successions are the rapid changes in thickness both across and along-strike the belt. To the east of the Montosa basement high, the syn-rift Jurassic successions consist of conglomerates, sandstones, and calcareous intercalations.

On the western edge of the basin, thick (2000 m) Paleocene volcanic and sedimentary synorogenic successions formed by red sandstones, conglomerates, ignimbrites, tuffs, and volcanic breccias rest unconformably on the syn-rift Mesozoic deposits (Fig. 2), while other Paleocene–Oligocene continental synorogenic successions cover the eastern flank of the Montosa basement high (Jensen, 1976; Moscoso et al., 2010; Martínez et al., 2012; Peña et al., 2013) (Fig. 2). Furthermore, Paleocene intrusions made of monzonites, granodiorites, diorites, and dacites (Peña et al., 2013) affect both the syn-rift Mesozoic and synorogenic deposits. Radiometric dating of tuffs and ignimbrites intercalated in the growth strata of the synorogenic successions have constrained the age of deformation to Late Cretaceous–Paleocene (78–60 Ma), matching some radiometric ages recently reported for the intrusives in this region (Peña et al., 2013).

1.2. Outline of structural styles

The Lautaro Basin comprises an array of NNE structures and many of them are associated with inverted and thrust faults. The main structure is located along the western section of the basin, comprising a NNE-trending long wavelength and west-vergent asymmetric anticline that extends for 20 km (Figs. 2 and 3d), and has been related to an inversion anticline (Martínez et al., 2012, 2015). This anticline mainly affects the Triassic and Jurassic syn-rift deposits, which show drastic changes in thickness along the fold, showing a typical wedge shape toward the western edge of the Lautaro Basin, as illustrated in Figs. 3d and 4. The overturned frontal limb of this anticline is truncated by the NNE Calquis Fault (Figs. 2–4), which corresponds to an east-dipping fault that represents the western master fault of the basin (Fig. 2). However, in some places, the superficial expression of this fault is obscured by small intrusive bodies (monzogranites, diorites), volcanic flows, and quartz veins emplaced along the fault trace (Fig. 2). The geometry of the anticline has been recently related to the positive reactivation of the Calquis Fault (Martínez et al., 2012). Moreover, the interaction of minor syn-extensional normal and thrust faults recognized in the hanging wall of the Calquis Faults have also confirmed tectonic inversion episodes for this basin.

The tectonic mode along the central and eastern sector of the basin is dominated by a series of thick-skinned west-dipping thrusts, such as the Jorquera, Pauna-La Estancilla, Iglesia Colorada, and Vizcachas Faults (Figs. 2 and 3) that cut both the Mesozoic syn-rift deposits and the granitic pre-rift basement of the basin, as well as some thin-skinned thrust faults (e.g., the El Chanco Thrust) that mainly affect the Mesozoic successions (Fig. 2). Most of these thick-skinned thrusts (e.g., Pauna-La Estancilla, Iglesia Colorada, and Vizcachas Faults) are characterized by the presence of footwall synclines adjacent to the fault traces (Figs. 2 and 3). North of the Copiapó River, the hanging-wall of these faults are frequently composed of wide blocks of pre-rift basement. In contrast, to the south, the structures are thin-skinned, except for the Iglesia Colorada and Vizcachas Faults, which involve a large granitic block of pre-rift basement (Figs. 2 and 3). In this sector, clear semi-circular and elongated shallow intrusions were also recognized to form part of the hanging wall of some thrust faults such as the Pauna-La Estancilla Fault (Figs. 2 and 3). Structural restorations carried out for these west-dipping thrusts suggest that they may have been formed by previous extensional systems (Martínez et al., 2015).

2. Analog modeling

2.1. Experimental procedure

In order to understand the interplay between the inversion structures and magmatism in the Lautaro Basin, we conducted a series of physical analog models simulating the simultaneous

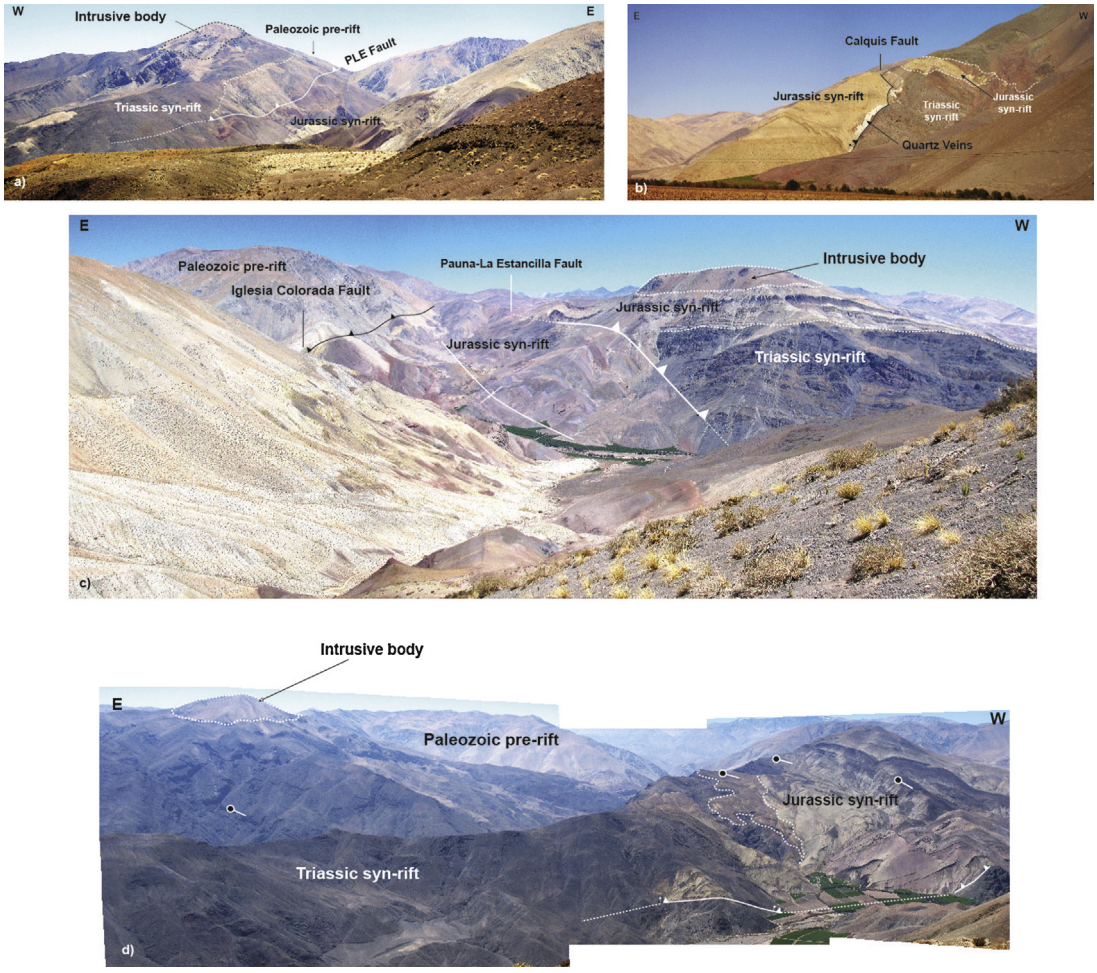

Fig. 3. (a) Aspect of the an intrusive body emplaced in the hanging wall of Pauna-La Estancilla (PLE) Fault, north of the Copiapó River; (b) transversal view of Calquis Fault showing evidence of magmatic migration along the fault trace; (c) panoramic view of opposite-verging PLE and Iglesia Colorada Faults, along eastern edge of Lautaro Basin. Note the intrusive body located in the hanging wall of PLE Fault; (d) E–W view of the inversion anticline exposed along central part of Lautaro Basin and aspect of intrusive body intruding the Mesozoic syn-rift deposits (see Fig. 2 for locations).

inversion of a half-graben structure and magma intrusion. The experiments were performed at the Tectonic Modeling Laboratory of the CNR-IGG and the Department of Earth Sciences in Florence, Italy, using a pure/simple-shear deformational apparatus (Fig. 5). Our models were inspired in the previous results presented by Bonini et al. (2012) who used a sand-microbeds-silicone models to reproduce the tectonic inversion of half-grabens and rollovers associated. Five sand–silicone models (Table 1) were deformed

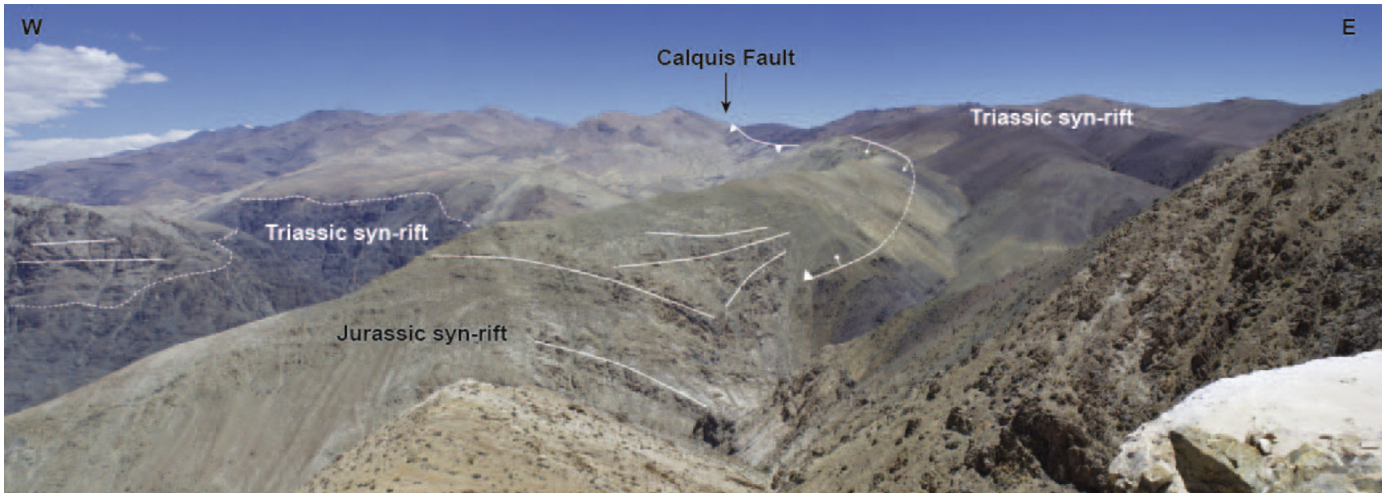

Fig. 4. W–E Panoramic view of Calquis Fault on western edge of Lautaro Basin, showing inversion anticline with "harpoon geometry" exposed in the hanging wall fault, and progressive unconformities developed in Jurassic marine syn-rift deposits (see Fig. 2 for location).

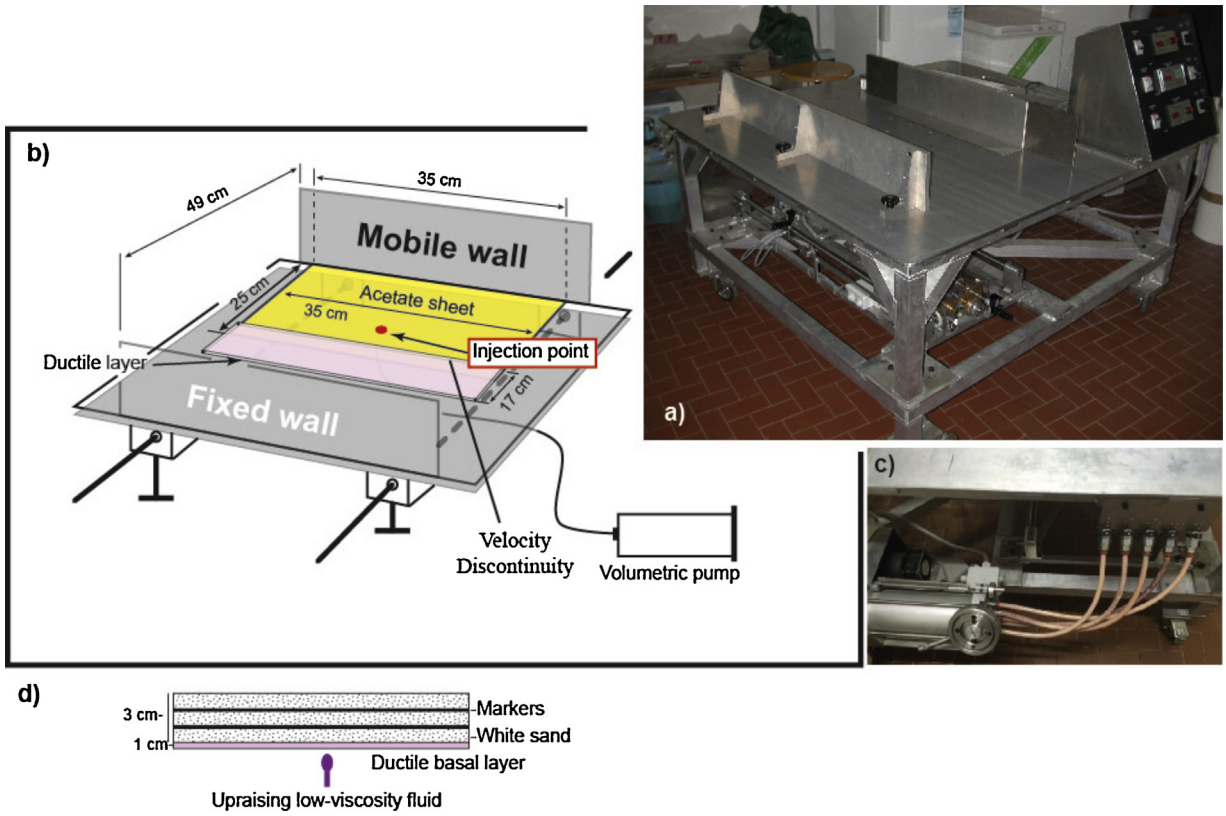

Fig. 5. (a) Photograph of deformation apparatus used in this study; (b) simplified experimental setup; (c) analog magma injection system; (d) model stratigraphy used in experiment.

by two successive phases, (1) first, an orthogonal extension creating a normal fault system that was followed by (2) a phase of coaxial and orthogonal shortening. The kinematic of the extension and shortening phases were similar to the previous experiments reported by Bonini et al. (2012), however; the shortening phase was accompanied by the injection of a viscous fluid to simulate magma emplacement. The extension and shortening of the models were obtained by lateral displacement of a mobile wall driven by a stepper motor controlled via a control panel (Fig. 5). A special injection apparatus formed by a piston and a magma distribution system consisting of cylindrical pipes (10 mm in diameter) allowed us to reproduce the magma injection during the shortening phase (Fig. 5c).

The models had initial dimensions of 35 cm × 49 cm × 4 cm, and were built above an acetate sheet (35 cm × 25 cm) attached to a mobile wall that created a velocity discontinuity (VD) at the base of the model (Fig. 5b and d). Our models were inspired in the knowledge of the vertical stratification of the Lautaro Basin. In order to reproduce geological conditions similar to those observed in this basin, the models consisted of a 1-cm-thick basal ductile layer of silicone to simulate a mobile ductile level under the basin. Over the basal ductile layer we used a 3-cm-thick package of colored sand to simulate the pre-rift basement of the basin (Fig. 5d). The first extension phase was identical in all models; each model was extended by 4 cm at a rate of 3 cm/h (Table 1) and syn-rift sedimentation was applied at convenient and regular time intervals in the main depocenters formed during the entire deformation obtaining a final fill of until 1.2 cm at the main depocenters (Fig. 6b). During the second phase, the models were shortened orthogonally to the VD by 4 cm to 6 cm (depending on the model) at a constant rate of 2 cm/h, together with the syn-shortening injection of the analog magma (Table 1). Syn-compressive sedimentation was applied only to model IM5 (Table 1). During this phase, the acetate sheet was released from the mobile wall to prevent folding of the acetate sheet during shortening. The analog magma was injected at a single point in the central part of the model, 4 cm from the edge of the acetate sheet (Fig. 5a), from a feeding pipe with a diameter of 0.9 cm. The injection was started after one hour of deformation; subsequently, the magma injection was concurrent with the deformation (Table 1). In the modeling, we also explored the effect of the injection rate by the deformation style acquired by the model as it was increasing. The injection rate varied from 20 cm/h to 40 cm/h depending on the model (Table 1), which corresponded to a magma flux of 12 and 25 cm^3/h, respectively. Top-view photographs were taken at regular time intervals during the experiments. Deformation of the model surface was monitored through fringe projection analysis, a technique that allows the determination out-of-plane displacements by projecting binary fringes over the model surface, and imaging it at different deformation stages (the difference in the corresponding optical phases defines the relative deformation between the two stages; Barrientos et al., 2008). This technique also allowed us to obtain 3D reconstruction of the deformation of the model surface (i.e., uplift or subsidence) at different stages of shortening, as well as final digital elevation models (DEMs) of that surface. Afterwards, the deformation models were soaked in water to allow the cutting of serial cross sections.

2.2. Model materials and scaling

The brittle behavior of rocks represented by the pre-rift basement and the infill of the Lautaro Basin was simulated by well-sorted dry-Qz sand with grain dimensions <250 μm, an angle of internal friction of 39°, cohesion of 66 Pa, and a density of 1550 kg m^{-3} (Schreurs et al., 2006). This material was deployed in a sand pack with different colored sand layers used as passive markers to visualize the internal deformation in the cross-sections

Table 1
Model characteristics for the experiments performed in this study.

Model	Tectonic inversion vs. magma injection										
	Initial dimension (cm)	Thickness (cm)	Test type	Material used	Extension E (cm)	Shortening S (cm)	Synorogenic sedimentation	Injection	Ve	Vs	Vi
1	35 length × 49 wide	3 with a weak basal layer of 1 cm	Orthogonal	Silicone and dry sand	4	4	No	After of first hour of S	3 cm/h	2 cm/h	20 cm/h
2	35 length × 49 wide	3 with a weak basal layer of 1 cm	Orthogonal	Silicone and dry sand	4	4	No	Simultaneous with S	3 cm/h	2 cm/h	20 cm/h
3	35 length × 49 wide	3 with a weak basal layer of 1 cm	Orthogonal	Silicone and dry sand	4	4	No	Simultaneous with S	3 cm/h	2 cm/h	40 cm/h
4	35 length × 49 wide	3 with a weak basal layer of 1 cm	Orthogonal	Silicone and dry sand	4	6	No	Simultaneous with S	3 cm/h	2 cm/h	40 cm/h
5	35 length × 49 wide	3 with a weak basal layer of 1 cm	Orthogonal	Silicone and dry sand	4	6	Yes	Simultaneous with S	3 cm/h	2 cm/h	40 cm/h

Ve: extension velocity.
Vs: shortening velocity.
Vi: injection velocity.

(Table 1). A basal ductile layer of Polydimethylsiloxane (PDMS) was introduced in the model as technical solution to distribute deformation. This transparent Newtonian silicone has a density of 965 kg m^{-3} and a viscosity of ~1.5 × 10^4 Pa s (e.g., Weijermars, 1986). The material used to reproduce the magmatic intrusions was a mixture of silicone putty (Mastic Silicone Rebodissant 29, produced by CRC, France) and Oleic Acid (4:1 in weight) resulting in a low-viscosity Newtonian fluid with viscosity of ~7 × 10^2 Pa s and density of ~1060 kg m^{-3} (Corti et al., 2005).

The models were scaled to achieve geometric, dynamic, and kinematic similarity (Hubbert, 1937; Ramberg, 1981). We used a length scaling ratio (l^*), where the asterisk denotes the ratio between the model and natural values) of 10^{-5}, such that 1 cm in the models corresponds to 1 km in nature Both the models and the natural case presented here are subject to the same value of gravitational acceleration, imposing a scale factor $g^* = 1$. On the other hand, the density ratio ρ^* is close to 0.5, as resulting from the ratio between the granular material used (~1550 kg m^{-3}) and the rocks (~2800 kg m^{-3}) (e.g., Schellart, 2000), and the ratio between our silicone mix (~1060 kg m^{-3}) and a natural granitic magma at the emplacement conditions (ca. 2400 kg m^{-3}; e.g., Montanari et al., 2010). This results in a stress scaling ratio: ($\sigma^* = \rho^* g^* l^*$) of ~5 × 10^{-6}. The stress scaling ratio is related to the scaling ratios of strain rate (ε^*), viscosity (η^*), and velocity of deformation (V^*), by the relationship $\sigma^* = \eta^* \varepsilon^* = \eta^* (V^*/l)$. This implies that the velocity of deformation in the models (2 cm/h) scales to natural values of ~5–50 mm/year for viscosities of a natural granitic magma varying between ~5 × 10^{17} and ~5 × 10^{16} Pa s. Thus, the silicone mix was only able to simulate a high viscosity magma with high crystal content (e.g., Román-Berdiel et al., 1997; Benn et al., 1998, 2000). However, this silicone mix was still suitable to model a significant strength contrast between the analog magma and the host rocks (Cruden et al., 1995). In the experimental conditions with slow displacement velocities, the silicone mix offers a negligible resistance and scaling for viscosity is not critical (Román-Berdiel et al., 1997). The scaling of the injection velocity results in natural values of injection rates between 0.05 and 1 m/year, in line with previous modeling works on magma emplacement (e.g., Corti et al., 2005). This results in a scaled magma flux of ca. 30 × 10^3 to 60 × 10^4 m^3/year, and a scaled volume of injected material between ca. 25 and 70 km^3. These values are reasonably similar to those obtained from the outcropping dimension of the plutons (Fig. 2). Since the scaling ratio of time (t^*) is related to the ε^* and V^* ratio ($t^* = 1/\varepsilon^* = l^*/V^*$), one hour of model deformation corresponds to ~0.04–0.4 Ma in nature.

2.3. Modeling limitations and simplifications

Analog models normally simplify the complexity of natural systems by introducing some limitations, in most cases with regard to the difficulty of correctly reproducing the thermal and rheological conditions. Specifically, modeling magma emplacement involves important limitations that essentially concern the rheological properties of the analog magma, the variations in rheology and strength during cooling and crystallization, and the emplacement rates (e.g., Corti et al., 2003; Merle, 2015). In our modeling procedure, an important simplification involves the rheological characteristics of the analog magma, which ignores the thermal effects and simulates a natural high-viscosity magma (~10^{17} Pa s). Other important limitation is related to the scaling of total volume of analog magma injected, since it is difficult to estimate how much was the total volume of magma accumulated in the Lautaro Basin during the compressive deformation. On the other hand, the consideration of a high-viscosity magma is a reasonable approximation, given that the analog magma is intended to model the emplacement of a granitic body at upper crustal levels. Another important factor

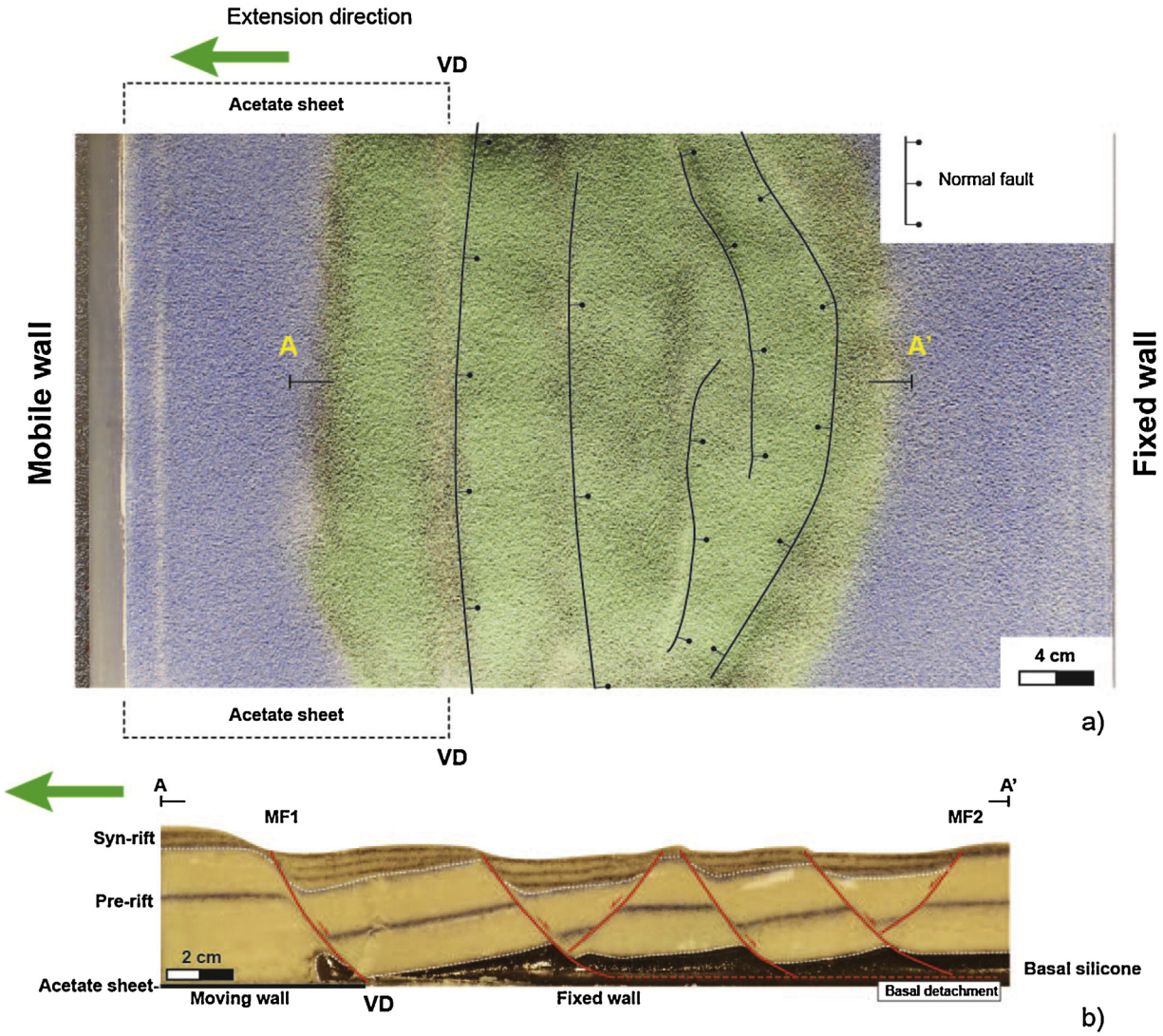

Fig. 6. (a) Interpreted top-view photo at the final state of the extensional model, illustrating direction of tectonic transport and final position of the velocity discontinuity = VD; (b) interpreted cross-section (A–A′) of photo at the end of deformation.

in the comparison between models and nature is related to the rate of magma emplacement. Some models of granite emplacement envisage injection rates several orders of magnitude higher than the deformation rates (e.g., Petford et al., 2000). In our modeling, the injection rate was only one order of magnitude higher (Table 1). However, in some cases, the migration of melts in natural shear zones may occur at rates similar to the regional tectonic deformation rates, for instance when granitic plutons are emplaced in successive magma pulses over a long time span (e.g., Glazner et al., 2004). In these cases, it is likely that previously emplaced magma will be partly or largely crystallized when later magma batches are emplaced (see also Benn et al., 1998, 2000). Another factor concerns the deformation apparatus, which consists of a 10-mm-wide injection point. This aperture scales down to 1 km in nature, and may simulate a pervasive zone of magma transport (e.g., Benn et al., 2000).

In spite of these limitations, a number of analog modeling studies have investigated—as a first approximation—the process of magma upwelling and emplacement in different tectonic environments, i.e., continental extension (Román-Berdiel, 1999; Bonini et al., 2001; Corti et al., 2003), transtension and strike-slip (Román-Berdiel et al., 1997, 2000; Corti et al., 2001, 2002, 2005), transpression (Benn et al., 1998, 2000), and compression (Galland et al., 2007; Montanari et al., 2010; Ferré et al., 2012). This study represents the first attempt to model the role of magma in analog models of inversion tectonics. As in previous experimental works, our results may provide a rough picture of the deformation outcome and contribute to unraveling the interactions between deformation and magma dynamics in these natural systems.

3. Results

3.1. First-phase extension

The extensional deformation imposed on each model was perpendicular to the velocity discontinuity, and the bulk displacement was invariably limited to 4 cm (Fig. 6). During this phase, the deformation was mainly accommodated by a series of four half-grabens characterized by a asymmetric geometry (Fig. 6). The master faults that bounded the half-grabens were generally continuous, with a strike roughly parallel to the velocity discontinuity (Fig. 6). Moreover, small and isolated transfer zones developed locally at the center of the half-graben to accommodate the extension deformation (Fig. 6). The extended models were characterized by synthetic and antithetic normal faults, dipping ~60° toward or away from the mobile wall, respectively (Fig. 6), and a

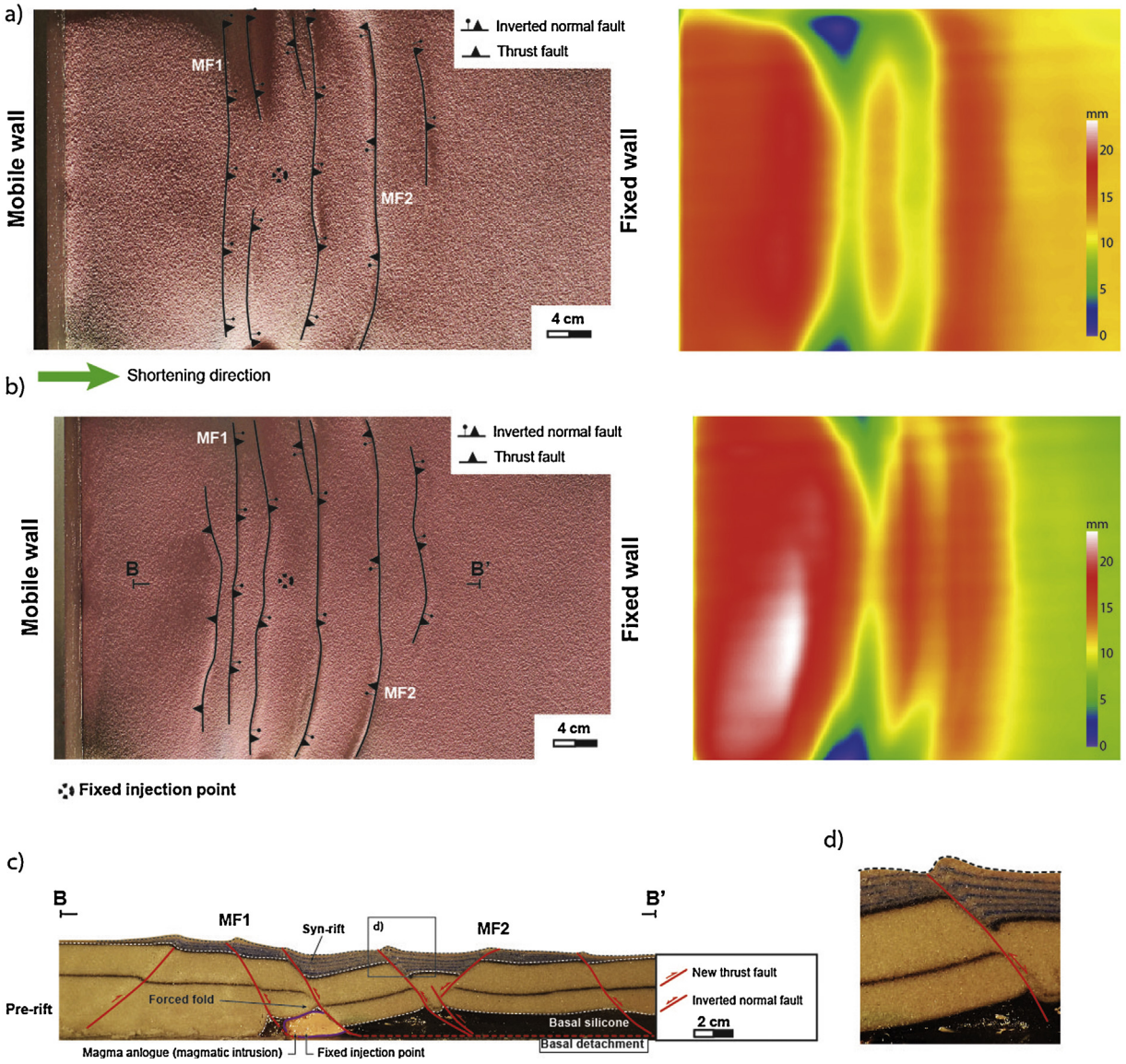

Fig. 7. Interpreted top-view photo (left panel) and digital elevation model of model surface (right panel) after 2 cm of shortening (a), and at final stage (b) of basin inversion model IM1. In top view, positions of inverted master faults M1 and M2 are indicated. (c) Interpreted cross-section (B–B′) of the photo and emplacement geometry observed at the end of deformation. (d) Detail of the "arrowhead or harpoon" geometry developed from the inversion of the previous normal faults.

structural horst separated the grabens. The faults were arranged parallel to one another in plan view; they had listric geometries, and rollover anticlines were formed in their hanging wall blocks (Fig. 6), similar to those reported by Mitra and Islam (1994). The half-grabens contained asymmetric syn-rift wedges, which thicken toward the master faults up to a maximum depth of ~2 cm (Fig. 7). Listric synthetic and antithetic master normal faults (M1 and M2) delimited the extensional zone that formed in this phase (Fig. 6).

3.2. Second-phase shortening and analog magma injection

Previously to run the experiments of the second phase (shortening and analog magma injection), a simple phase of pure orthogonal shortening without magma injection was carried out. The results were basically similar to those obtained by Bonini et al. (2012). During the second-phase, both the master and the subsidiary faults were partially reactivated in different degrees, and propagated upwards to affect the complete syn-rift sequence (Figs. 7–11). This resulted in the partial closure of the half-grabens, as well as in the reverse displacement and folding of the pre-rift and syn-rift sequences along the reactivated faults, and thickening of the sand pack and basal ductile layer (Figs. 7–11). The compressive deformation was mainly accommodated by displacement and back rotation of the hanging wall blocks and by the pushing of individual syn-rift wedge by the reactivation of synthetic faults that resemble the geometry of the "arrowhead or harpoon" structures described in the experiments of Buchanan and McClay (1992).

Different geometrical relationships between the magmatic intrusion and the reactivated structures developed depending on the timing of the magma injection (i.e., after the shortening or coevally with it) and on the relative rates of intrusion and shortening. In particular, when the magma injection was applied after one hour of shortening (Model IM1; Fig. 7; Table 1), the analog magma was emplaced vertically at the base of the pre-rift hanging wall block of the master fault MF1, producing a forced fold (Fig. 7c). The almost linear and uninterrupted shape of the faults highlighted by top-view photos suggests no major influence played by intrusion

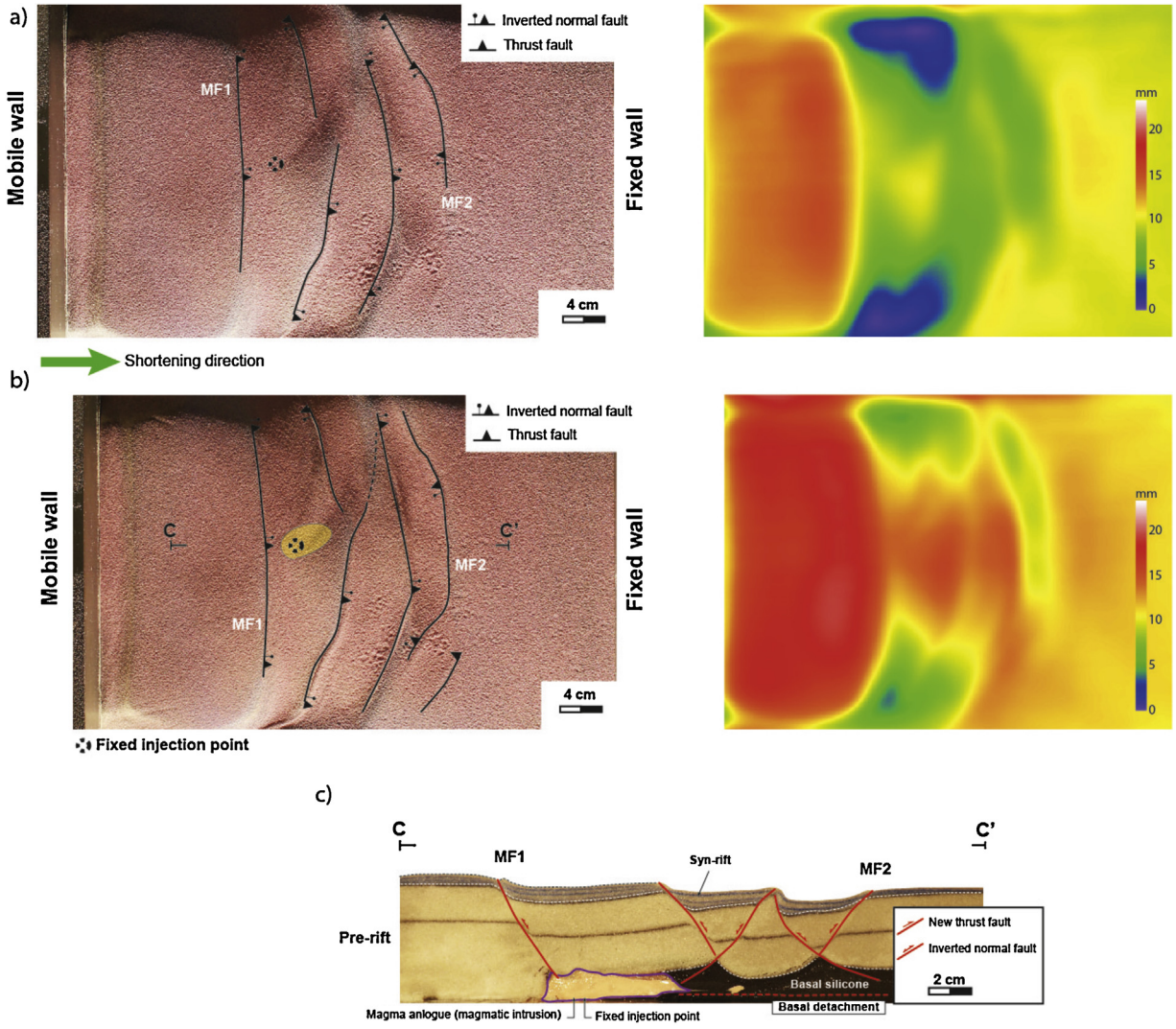

Fig. 8. Interpreted top-view photo (left panel) and digital elevation model of model surface (right panel) after 2 cm of shortening (a), and at final stage (b) of basin inversion model IM1. In top view, positions of inverted master faults M1 and M2 are indicated. (c) Interpreted cross-section (C–C′) of the photo and emplacement geometry observed at the end of deformation. Geometry of uplifted area is indicated in yellow. (For interpretation of the references to color in this figure legend, the reader is referred to the web version of this article.)

on the plan-view geometry of the structures (Fig. 7a and b). This occurred because the intrusion was generated late respect to the structural configuration.

Similarly, uplift of the model surface is mostly localized above the major structures and at the moving wall, with an almost linear pattern following the trend of reactivated faults (Fig. 7a and b). This again indicates no major influence of the intrusion on the pattern of deformation of the model surface. Synchronous shortening and magma injection (Model IM2; Table 1) resulted in a general arcuate shape to the structures, except for the main master fault MF1 that instead maintained a straight trace (Fig. 8a and b). In this case, uplift of the model surface was located away from the mobile wall and mostly localized above the reactivated master fault, as well as above the intruding magma (Fig. 8a and b). In cross-section, the magmatic intrusion acquired a sill geometry, which was emplaced along the lower section of the master fault MF1, and preferentially migrated forward along the base of the sand pack where some of the inverted faults nucleate (Fig. 8c). This forward migration of the analog magma favored the reactivation of some normal faults, particularly those rooted at the tip of the intrusion (Fig. 8c). As a consequence, these inverted faults propagated forward more than the master fault, which was less influenced by intrusion.

Models IM3–IM5 were conducted with a higher injection rate (40 cm/h; Table 1), which also corresponded to a higher volume of injected material, and thus provide information on the role of these parameters in the structural evolution of the system. In model IM3, the final structural geometry resembled that of model IM2, with the prominent arcuate shape of the synthetic fault MF2, and the roughly linear shape of fault MF1. A pronounced dome developed over the injection point zone during shortening in this model (Fig. 9a and b), and a radial fracture network formed at the crest of the dome (Fig. 9ca, b). Similar to model IM2, the analog magma preferentially migrated forward along the base of the brittle crust, promoting the propagation of the structures rooted at its edges, and thus controlling their overall arcuate shape (Fig. 9). Some analog magma rose through the master fault MF1 (Fig. 9c). The increase in the injection velocity resulted in an increase in the volume of intruded material, which in turn gave rise to a significant uplift of both the base of the experimental brittle crust and the model surface (Fig. 9c).

Model IM4 was shortened by 6 cm, and—as in previous models—deformation was accommodated by partial reactivation and rotation of the master and subsidiary faults; the plan-view pattern of deformation at the end of the model consisted of straight (MF1) and semi-arcuate inverted secondary faults, as well as some

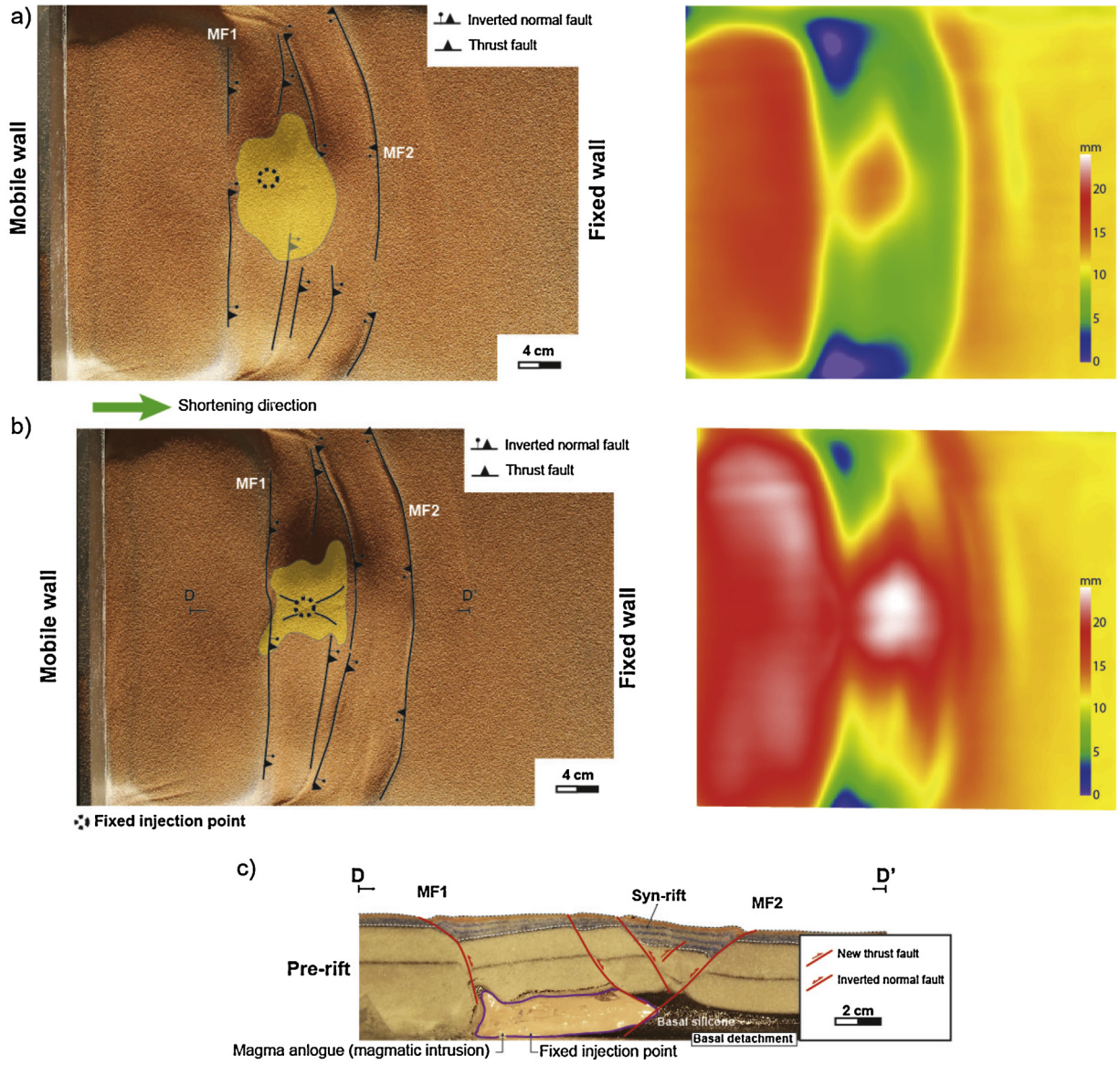

Fig. 9. Interpreted top-view photo (left panel) and digital elevation model of model surface (right panel) after 2 cm of shortening (a), and at final stage (b) of basin inversion model IM1. In top view, positions of inverted master faults M1 and M2 are indicated. (c) Interpreted cross-section (D–D′) of the photo and emplacement geometry observed at the end of deformation. Geometry of uplifted area is indicated in yellow. (For interpretation of the references to color in this figure legend, the reader is referred to the web version of this article.)

new minor thrusts (Fig. 10a and b; Table 1). Similar to previous models, magma migrated both forward at the base of the brittle crust and subordinately upwards along the fault MF1; this gave rise to significant doming of the region above the injection point (Fig. 10). However, the increased shortening in this model resulted in a clear asymmetrical shape of the dome, associated with a large asymmetric inversion anticline in the central part of the model (Fig. 10c). The folding resulted from the reactivation of previous faults, expressed by the fault-propagation style, and newly formed thrusts (Fig. 10c). The higher duration of the shortening phase with respect model IM3 resulted in an increase in the volume of intruded material, which in turn resulted in a pronounced doming of the model surface (Fig. 10c).

Finally, in order to test the influence of the synorogenic sedimentation in the final geometry of the magmatic intrusion, we ran a last model (model IM5) characterized by simultaneous shortening, magma injection, and a high rate of sedimentation (Fig. 11; Table 1), which was applied as deformation fronts were formed. This experiment resulted in an essentially symmetrical dome localized over the injection point, and was limited by the inverted master fault MF1 and other inverted antithetic faults, (Fig. 11a and b). Two oppositely verging thrusts developed in the central part of this uplifted zone (Fig. 11a and b). The model cross-section confirmed that the analog magma migrated forward horizontally and subordinately vertically along the inverted master fault MF1. However, in model IM5, a more limited vertical migration of the analog magma was observed, possibly in relation to the loading of synorogenic sedimentation. Similarly to model IM4, the presence of the magma favored major slips during the reactivation of the faults, as well as the folding in the central part of the model (Fig. 11c). As in previous models, during the shortening, the fault blocks were folded and the fault systems were partially inverted. A broad "pop-up" structure developed in the central part of the model bounded by the inverted master faults MF1 and MF2, and was characterized by a drastic lateral changes in thickness of the synorogenic strata, which thickened away from the uplifted inversion anticline (Fig. 11c).

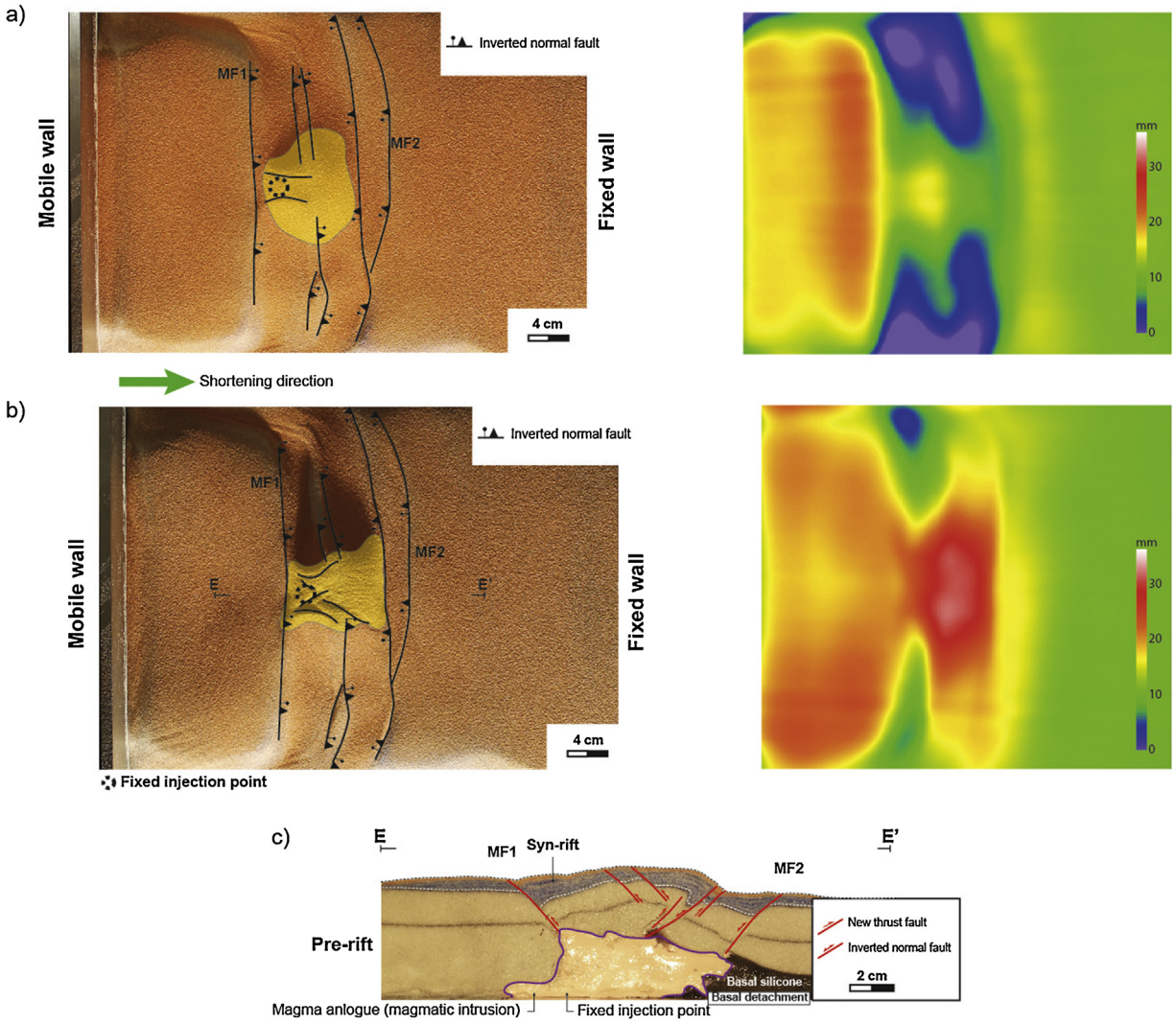

Fig. 10. Interpreted top-view photo (left panel) and digital elevation model of model surface (right panel) after 2 cm of shortening (a) and at final stage (b) of basin inversion model IM1. In top view, positions of inverted master faults M1 and M2 are indicated. (c) Interpreted cross-section (E–E′) of the photo and emplacement geometry observed at the end of deformation. Geometry of uplifted area is indicated in yellow. (For interpretation of the references to color in this figure legend, the reader is referred to the web version of this article.)

4. Discussion

In northern Chile, the occurrence of intrusive bodies in the hanging wall and footwall of thrust fault systems has been largely recognized as a common structural style derived from simultaneous shortening and magmatism (e.g., Moscoso and Mpodozis, 1988; Mpodozis and Ramos, 1989; Cornejo and Mpodozis, 1996; Arévalo, 2005; Amilibia et al., 2008; Peña et al., 2013), however; today also is accepted the occurrence of intrusive bodies along inverted faults, which appear to have exerted the main control to the emplacement of magmatic intrusions during the tectonic inversion of the Mesozoic basins (Amilibia et al., 2008; Martínez et al., 2012, 2015). Considering this last tectonic scenario, the analog models presented here provide a first approach to help understand the geological elements formed during the progressive shortening of a pre-existing extensional system, and magma emplacement, therefore we recommend take these only as broad insights to analyze some tectonic settings dominated by inverted structures and intrusive bodies. Although our experiments necessarily involve some important simplifications, particularly those related to temperature variations during the deformation (the models approximate the thermo-mechanical process to a merely mechanical process) and the effects of fluid pressure on faulting, the results provide valuable qualitative insights into the process.

4.1. Inversion of a previous extensional system

The geometry of inverted structures obtained in this work almost invariably shows a clear positive reactivation and upward propagation of a set of listric and normal faults. The latter show partial and simple reactivation, similar to those observed in tectonic inversion models built with purely brittle materials (e.g., Koopman et al., 1987; Buchanan and McClay, 1992; Eisenstadt and Withjack, 1995; Panien et al., 2005). During the tectonic inversion, the reactivated faults rotated progressively to steeper dips. Individual pre-rift fault blocks and the syn-rift successions were folded and uplifted, and were frequently buttressed against the faults, acquiring "harpoon" geometries, consistent with those reported by Buchanan and McClay (1992). Similar to previous experimental results using brittle–ductile models (e.g., Mitra and Islam, 1994; Brun and Nalpas, 1996; Bonini, 1998; Bonini et al., 2012; Di Domenica et al.,

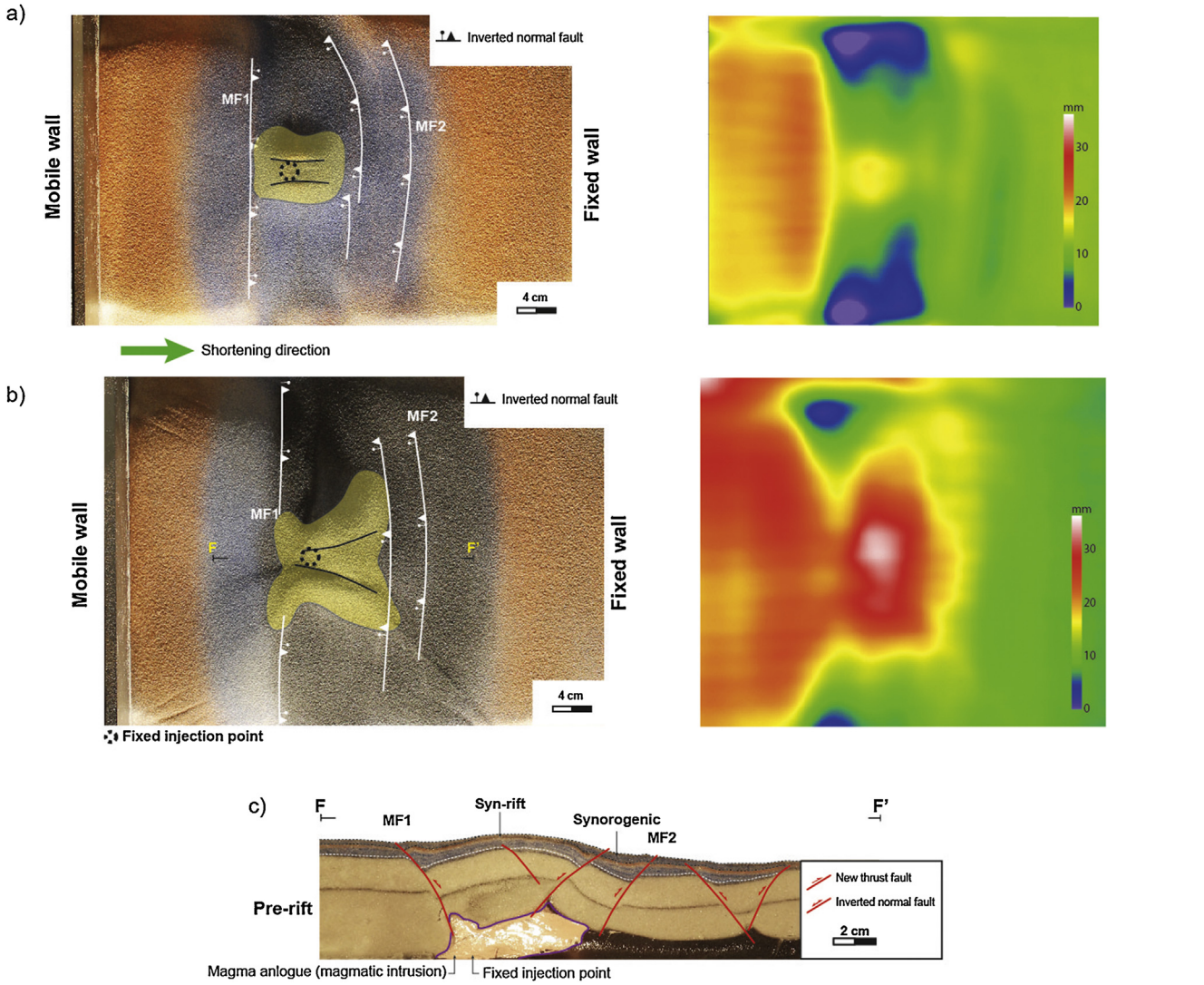

Fig. 11. Interpreted top view photo (left panel) and digital elevation model of model surface (right panel) after 2 cm of shortening (a), and at final stage (b) of basin inversion model IM1. In top view, positions of inverted master faults M1 and M2 are indicated. (c) Interpreted cross-section (F–F′) of the photo and emplacement geometry observed at the end of deformation. Geometry of uplifted area is indicated in yellow. (For interpretation of the references to color in this figure legend, the reader is referred to the web version of this article.)

2014), a set of asymmetrical anticlines developed during the inversion phase on the hanging wall of the master faults (MF1 and MF2), which frequently rotated more than those localized within the extensional system. Unlike other models deformed by orthogonal inversion (Dubois et al., 2002), the complete reactivation does not result in the formation of footwall shortcuts. This might be related to the fact that the reverse displacement does not exceed the earlier extensional displacement, and deformation is mainly accommodated by folding and tilting of the fault hanging wall. Some authors have argued that the tectonic inversion is more difficult during orthogonal compression (e.g., Lowell, 1995). However, our results suggest that orthogonal reactivation is facilitated when the faults have moderate dips (40–60°) (e.g., Sibson, 1995; Bonini et al., 2012).

4.2. Relationships between tectonic inversion and magma emplacement

Previous analog models have demonstrated that the geometry of magmatic intrusions is strongly related to the deformation modes that may characterize the upper crust (Román-Berdiel et al., 1997, 2000; Galland et al., 2003; Benn et al., 2000; Corti et al., 2005; Montanari et al., 2010). This situation has also been identified through multiscale geological observations of the magmatic intrusions in some inverted basins in northern Chile (Amilibia and Skarmeta, 2003; Amilibia et al., 2008; Martínez et al., 2013; Peña et al., 2013).

Although we have carried out limited tests, we suggest that factors such as the timing of the intrusion, the shortening vs. injection rates and the volumes of injected material, as well as a high synorogenic sedimentation may affect the final geometry (Figs. 8–11). In particular, almost no influence of magma intrusion on the structural architecture is observed when magma is injected after shortening has been well established, and structures have already acquired a preferred architecture before magma enters the system. When the two processes are contemporaneous, there is significant interplay between magma emplacement and structural evolution. Magma preferentially migrates forward in a horizontal direction, facilitating the advancement of the reactivated structures rooted at the tips of the intrusion; as a consequence, these reactivated structures acquire a prominent arcuate shape. Minor magma upwelling occurs at the base of the more internal master fault (MF1), which maintains a rather linear shape in plan view. Magma intrusion is always associated with a prominent upwelling of the model surface because space for magma is created by folding of the overlying brittle crust,

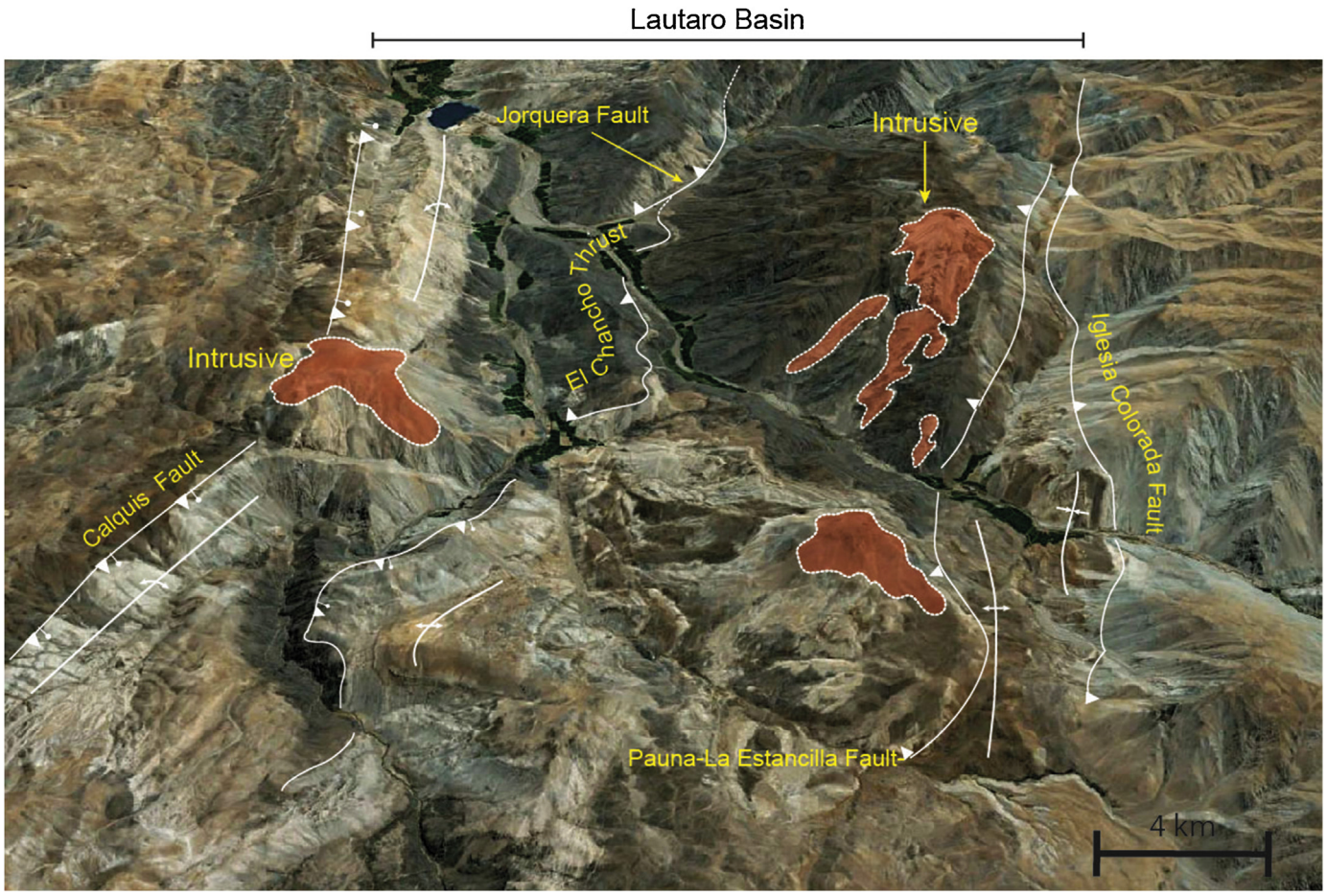

Fig. 12. Interpreted oblique Google Earth® (http://earth.google.it/download-earth.html) view of Lautaro Basin, showing disposition of main fault systems recognized in the region and their relationships with the magmatic intrusions.

a process which is dependent on the volume of injected material. An increase in this parameter (which may be related to either an increase in injection velocity and/or a longer shortening phase) gives rise to a more prominent folding of the brittle crust (associated with large, often asymmetric, anticlines) and consequently a more pronounced surface doming. Model results thus indicate that the ratio between the magma injection rate and deformation rate mainly controls the final top-view and cross-section geometry of the intrusions, in line with previous experiments by Galland et al. (2009), Ferré et al. (2012), Mazzarini et al. (2010), and Montanari et al. (2010).

4.3. Comparison with the Lautaro Basin

We have compared our results with those geological evidences of inverted faults and magmatic intrusion recognized in the Lautaro Basin. It is worth noting that we only have made a qualitative comparison between the structural and intrusive geometries and the model presented, however; this comparation can be limited, because this is conditioned by factors such as the limited exposure of intrusive bodies or the relationships between intrusives and inverted faults (Benn et al., 2000). Other results related to kinematic conditions result difficult to compare, because we observed final geometries. As discussed earlier, the structure of the Lautaro Basin shows a number of features indicating that magmatism and shortening occurred simultaneously. This situation is good illustrated in Fig. 12, where the main intrusive bodies are emplaced along the reactivated master fault (Calquis Fault), the hanging wall of the arcuate Pauna-La Estancilla Fault, as well as the anticlines associated with both structures. These intrusions correspond to Paleocene–Eocene monzonites and hypabyssal rocks, which show an elongated form in plan view (Fig. 12).

In first place our experiments showed that the intrusions migrated horizontally toward the inversion anticlines associated with reactivated faults confined in the margins of an inverted basin, but also occurred along the basal sections of reactivated master faults. This situation is geometrically comparable with the geological observations in the Lautaro Basin related to the occurrence of intrusive bodies along the Calquis and Pauna-La Estancilla Fault, because both structures represent the western and eastern border faults of an inverted half graben (Fig. 12). In this sense, it is possible to speculate that the magmatic intrusions migrated toward the edge of the basin during the Andean deformation. On the other hand, our models showed that a notable uplift developed in the central sector of the basin as a result of the shortening and simultaneous injection of magma. The surface uplift related to magma emplacement is strongly dependent on the volume of the injected material, and thus surface doming may be overestimated in those models with the maximum intruded volume. Other similarities may be related to the plan-view geometry of the faults. In the models the arcuate shape reproduced by the central inverted faults resulted from coeval shortening and magmatism. This pattern is similar to those displayed by the central fault systems of the Lautaro Basin, which also resulted of shortening, reactivation of previous normal faults and magmatism (Martínez et al., 2015) (Fig. 12). Although some of these structures were previously interpreted as thrust faults (Jensen, 1976; Moscoso and Mpodozis, 1988; Arévalo, 2005), recent interpretations based on

balanced cross-sections suggest that these correspond to inverted structures (Martínez et al., 2015). Finally, the Calquis Fault, which trends N–S, exhibits a straight geometry which is very similar to that of the model master fault MF1, and the inversion anticline related to the Calquis Fault is strikingly comparable to the anticline developed on the MF1 hanging wall.

5. Conclusions

The Lautaro Basin in northern Chile (27–28° S) exhibits a particular tectonic inversion style, which is essentially controlled by the tectonic inversion of Jurassic extensional structures. The Andean deformation superimposed on these extensional systems lead to the development of inversion anticlines with "harpoon geometry", as well as other thrust faults and folds that correspond to both partially reactivated normal faults and new thick-skinned thrusts. Our sand–silicone models simulate a scenario characterized by the synchronous tectonic inversion magma injection of a half-graben previously formed during an extensional phase, enabling direct comparisons with the Lautaro Basin. The results obtained here provide some hints on the coeval processes of tectonic inversion and magma emplacement. The features observed in nature and explained by our models indicate that:

The tectonic style of the Lautaro Basin in northern Chile is dominated by a clear interplay of inverted structures, thrust faults and intrusive bodies, which appear to have resulted of synchronous shortening and magmatism.

Within the basin intrusive bodies are preferentially located along inversion anticlines and inverted faults, with intrusions influencing the final geometries (top-view and cross-section) of inverted normal faults.

Syn-inversion magmatism may favor major slip on the structures, which could be associated with major lubrication of the faults during their reactivation, Based on this, high rates of magmatism during basin inversion could favor the crustal thickening and doming.

Although not systematically tested, our results suggest that synorogenic sedimentation may influence fault reactivation and consequently the final geometry of the syn-inversion intrusions.

Acknowledgements

We thank the Editor W. Schellart and an anonymous reviewer for the several constructive comments that helped to improve the manuscript. This work was supported by the National Fund for Scientific and Technological Development FONDECYT grant no. 3140557, "The crustal structure and timing deformation along the Chilean flat-slab subduction segment (27–29° S), Central Andes". The authors thank S. Villagran and M. Vaccaris for fieldwork assistance. We are also indebted to Dr. Constantino Mpodozis for many fruitful discussions on Andean tectonics.

References

Aguirre-Urreta, M.B., 1993. Neocomian ammonite biostratigraphy of the Andean basins of Argentina and Chile. Rev. Esp. Paleontol. 8, 57–74.
Allmendinger, R.W., Jordan, T.E., Kay, S.M., Isacks, B.L., 1997. The evolution of the Altiplano-Puna Plateau of the Central Andes. Annu. Rev. Earth Planet. Sci. 25, 139–174.
Amilibia, A., Skarmeta, J., 2003. La inversión tectónica en la Cordillera de Domeyko en el norte de Chile y su relación con la intrusión de sistemas porfídicos Cu-Mo. In: Paper presented at X Congreso Geológico Chileno, Concepción.
Amilibia, A., Sàbat, F., McClay, K.R., Muñoz, J.A., Roca, E., Chong, G., 2008. The role of inherited tectono-sedimentary architecture in the development of the central Andean mountain belt: Insights from the Cordillera de Domeyko. J. Struct. Geol. 30, 1520–1539.
Anderson, E.M., 1951. The Dynamics of Faulting. Oliver and Boyd, Edinburgh.
Arévalo, C., Rivera, O., Iriarte, S., Mpodozis, C., 1994. Cuencas extensionales y campos de calderas del Cretácico Superior-Terciario Inferior en la Precordillera de Copiapó (27°–28° S), Chile. Paper presented at I Congreso Geológico Chileno, vol. 7., pp. 1288–1292.
Arévalo, C., 2005. Carta Copiapó, Región de Atacama. Servicio Nacional de Geología y Minería, scale: 1:100.000.
Arriagada, C., Cobbold, P., Roperch, P., 2006. Salar de Atacama basin: a record of compressional tectonics in the Central Andes since the mid-Cretaceous. Tectonics 25, 1–19.
Barrientos, B., Cerca, M., Garcia-Marquez, J., Hernandez-Bernal, C., 2008. Three-dimensional displacement fields measured in a deforming granular-media surface by combined fringe projection and speckle photography. J. Opt. A: Pure Appl. Opt. 10, 104027, http://dx.doi.org/10.1088/1464-4258/10/10/104027.
Barton, M.D., 1990. In: Anderson, J.L. (Ed.), The Nature and Origin of Cordilleran Magmatism, vol. 174. Geological Society of America, pp. 283–302.
Benn, K., Odonne, F., de Saint Blanquat, M., 1998. Pluton emplacement during transpression in brittle crust: new views from analogue experiments. Geology 26, 1079–1082.
Benn, K., Odonne, F., Lee, S.K.Y., Darcovich, K., 2000. Analogue models of pluton emplacement during transpression in brittle and ductile crust. Trans. R. Soc. Edinb. Earth Sci. 91 (Hutton IV special issue), 111–121.
Bonini, M., 1998. Chronology of deformation and analogue modelling of the Plio-Pleistocene 'Tiber Basin': implications for the evolution of the Northern Apennines (Italy). Tectonophysics 285, 147–165.
Bonini, M., Sokoutis, D., Mulugeta, G., Boccaletti, M., Corti, G., Innocenti, F., Manetti, P., Mazzarini, F., 2001. Dynamics of magma emplacement in centrifuge models of continental extension with implications for flank volcanism. Tectonics 20, 1053–1065.
Bonini, M., Sani, F., Antonielli, B., 2012. Basin inversion and contractional reactivation of inherent normal faults: a review based on previous and new experimental models. Tectonophysics 522, 55–88.
Brun, J.P., Nalpas, T., 1996. Graben inversion in nature and experiments. Tectonics 15, 677–687.
Buchanan, P.G., McClay, K.R., 1992. Experiments on basin inversion above reactivated domino faults. Mar. Petrol. Geol. 9, 486–500.
Charrier, R., Farías, M., Maksaev, V., 2009. Evolución tectónica, paleogeográfica y metalogénica durante el Cenozoico en los Andes de Chile norte y central e implicaciones para las regiones adyacentes de Bolivia y Argentina. Rev. Geol. Argent. 65, 5–35.
Clavero, J.E., Sparks, R.S.J., Pringle, M.S., Polanco, E., Gardeweg, M.C., 2004. Evolution and volcanic hazards of Taapaca Volcanic Complex, Central Andes of Northern Chile. J. Geol. Soc. 161, 603–618 (London).
Cornejo, P., Mpodozis, C., Ramírez, C., Tomlinson, A., 1993. Estudio geológico de la Región de Potrerillos y El Salvador (26°–27° Lat. S), Reg. Rep. IR-93-01, 2. Servicio Nacional de Geología y Minería 12, scale: 1:50.000.
Cornejo, P., Mpodozis, C., 1996. Geología de la Región de Sierra Exploradora (25°–26° S). Servicio Nacional de Geología y Minería, Informe Registrado IR 96-09,1, 330 p.
Corti, G., Bonini, M., Innocenti, F., Manetti, P., Mulugeta, G., 2001. Centrifuge models simulating magma emplacement during oblique rifting. J. Geodyn. 31, 557–576.
Corti, G., Bonini, M., Mazzarini, F., Boccaletti, M., Innocenti, F., Manetti, P., Mulugeta, G., Sokoutis, D., 2002. Magma-induced strain localization in centrifuge models of transfer zones. Tectonophysics 348, 205–218.
Corti, G., Bonini, M., Conticelli, S., Innocenti, F., Manetti, P., Sokoutis, D., 2003. Analogue modelling of continental extension: a review focused on the relations between the patterns of deformation and the presence of magma. Earth Sci. Rev. 63, 169–247.
Corti, G., Moratti, G., Sani, F., 2005. Relations between surface faulting and granite intrusions in analogue models of strike-slip deformation. J. Struct. Geol. 27, 1547–1562.
Cruden, A.R., Koyi, H., Schmeling, H., 1995. Diapiric basal entrainment of mafic into felsic magma. Earth Planet. Sci. Lett. 131, 321–340.
DeCelles, P.G., Ducea, M., Kapp, P., Zandt, G., 2009. Cyclicity in cordilleran orogenic systems. Nat. Geosci. 2, 251–257.
Di Domenica, A., Bonini, L., Calamita, F., Toscani, G., Galuppo, C., Seno, S., 2014. Analogue modeling of positive inversion tectonics along differently oriented pre-thrusting normal faults: an application to the Central-Northern Apennines of Italy. GSA Bull. 126, 943–955.
Dubois, A., Odonne, F., Massonnat, G., Lebourg, T., Fabre, R., 2002. Analogue modelling of fault reactivation: tectonic inversion and oblique remobilisation of grabens. J. Struct. Geol. 24, 1741–1752.
Eisenstadt, G., Withjack, M.O., 1995. Estimating inversion: results from clay models. In: Buchanan, J.G., Buchanan, P.G. (Eds.), Basin Inversion. Geological Society of London Special Publication, pp. 119–136.
Ernst, W.G., 1992. In: Burchfiel, B.C., Lipman, P.W., Zoback, M.L. (Eds.), The Cordilleran Orog: Conterminous U.S. Geological Society of America, pp. 515–538.
Ferré, E., Galland, O., Montanari, D., Kalakay, T., 2012. Granite magma migration and emplacement along thrusts. Int. J. Earth Sci., http://dx.doi.org/10.1007/s00531-012-0747-6 (Geol Rundsch).
Galland, O., Cobbold, P.R., de Bremond d'Ars, J., Hallot, E., 2003. Physical models of magmatic intrusion during thrusting. Terra Nova 15, 405–409.
Galland, O., de Bremond d'Ars, J., Cobbold, P.R., Hallot, E., 2007. Rise and emplacement of magma during horizontal shortening of the brittle crust: insights from experimental modelling. J. Geophys. Res. 112, http://dx.doi.org/10.1029/2006JB004604.

Galland, O., Planke, S., Neumann, E.-R., Malthe-Sørenssen, A., 2009. Experimental modelling of shallow magma emplacement: application to saucer-shaped intrusions. Earth Planet. Sci. Lett. 277, 373–383.
Glazner, A.F., Bartley, J.M., Coleman, D.S., Gray, W., Taylor, R.Z., 2004. Are plutons assembled over millions of years by amalgamation from small magma chambers? GSA Today 14, http://dx.doi.org/10.1130/1052-5173.
Godoy, E., Davidson, J.D., 1976. Pilares en compresión de edad Mioceno superior en los Andes del Norte de Chile (22°–30° Latitud Sur). Paper presented at I Congreso Geológico Chileno, vol. 1., pp. 87–103.
Godoy, E., Yán˜ez, G., Vera, E., 1999. Inversion of an Oligocene volcano-tectonic basin and uplifting of its superimposed Miocene magmatic arc in the Chilean Central Andes: first seismic and gravity evidences. Tectonophysics 306, 217–236.
González, G., Cembrano, J., Aron, F., Veloso, E., Shyu, B., 2009. Coeval compressional deformation and volcanism in the Central Andes, case studies from northern Chile (23°S–24° S). Tectonics 28, http://dx.doi.org/10.1029/2009TC002538.
Hubbert, M.K., 1937. Theory of scale models as applied to the study of geologic structures. Geol. Soc. Am. Bull. 48, 1459–1520.
Jensen, O., 1976. Geología de las nacientes del río Copiapó, entre los 27°53′ y 28°20′ de latitud Sur, provincia de Atacama, Chile. Memoria de Titulo (Inédito), Universidad de Chile, Departamento de Geología, pp. 249.
Koopman, A., Speksnijder, A., Horsfield, W.T., 1987. Sandbox model studies of inversion tectonics. In: Ziegler, P.A. (Ed.), Compressional Intra-plate Deformations in the Alpine Foreland, vol. 137. Tectonophysics, pp. 379–388.
Kozlowski, E.E., Cruz, C.E., Sylwan, C.A., 1996. Geología estructural de la zona de Chos Malal, Cuenca Neuquina, Argentina. In: Paper presented at XIII Congreso Geológico Argentino y III Congreso de Exploración de Hidrocarburos., pp. 15–26.
Lowell, J., 1995. Mechanics of basin inversion from worldwide examples. In: Buchanan, J.G., Buchanan, P.G. (Eds.), Basin Inversion, vol. 88. Geological Society of London Special Publication, pp. 3–19.
Maksaev, V., Zentilli, M., 1999. Fission track thermochronology of the Domeyko Cordillera, northern Chile: implications for Andean tectonics and porphyry copper metallogenesis. Explor. Min. Geol. 8, 65–89.
Martínez, F., Arriagada, C., Mpodozis, C., Peña, M., 2012. The Lautaro Basin: a record of inversion tectonics northern Chile. Andean Geol. 39, 258–278.
Martínez, F., Arriagada, C., Peña, M., Del Real, I., Deckart, K., 2013. The structure of the Chañarcillo Basin: an example of tectonic inversion in the Atacama region, northern Chile. J. S. Am. Earth Sci. 42, 1–16.
Martínez, F., Arriagada, C., Valdivia, R., Deckart, K., Peña, M., 2015. Geometry and kinematics of the Andean thick-skinned thrust systems: Insights from the Chilean Frontal Cordillera (28°–28.5° S) Central Andes. J. S. Am. Earth Sci., http://dx.doi.org/10.1016/j.jsames.2015.05.001.
Mazzarini, F., Musumeci, G., Montanari, D., Corti, G., 2010. Relations between deformation and upper crustal magma emplacement in laboratory physical models. Tectonophysics 484, 139–146.
Merle, O., 2015. The scaling of experiments on volcanic systems. Front. Earth Sci. 3, 26, http://dx.doi.org/10.3389/feart.2015.00026.
Mitra, S., Islam, Q.T., 1994. Experimental (clay) models of inversion structures. Tectonophysics 230, 211–222.
Montanari, D., Corti, G., Sani, F., Del Ventisette, C., Bonini, M., Moratti, G., 2010. Experimental investigation on granite emplacement during shortening. Tectonophysics 484, 147–155.
Moscoso, R., Mpodozis, C., 1988. Estilos estructurales en el Norte chico de Chile (28°–31° S), regiones de Atacama y Coquimbo. Rev. Geol. Chile 15, 155–158.
Moscoso, R., Mpodozis, C., Nassi, C., Ribba, L., Arévalo, C. (Compilador), 2010. Geología de la Hoja El Tránsito, Región de Atacama, Servicio Nacional de Geología y Minería de Chile, Serie Preliminar, 7, scale 1:250.000.
Mpodozis, C., Ramos, V.A., 1989. The Andes of Chile and Argentina. In: Ericksen, G.E., Cañas Pinochet, M.T., Reinemud, J.A. (Eds.), Geology of the Andes and Its Relation to Hydrocarbon and Mineral Resources Circumpacific Council for Energy and Mineral Resources, vol. 11. Earth Sciences Series, pp. 59–90.
Mpodozis, C., Kay, S., 1990. Provincias magmáticas ácidas y evolución tectónica de Gondwana: Andes chilenos (28–31° S). Rev. Geol. Chile 17, 153–180.
Mpodozis, C., Arriagada, C., Basso, P., Roperch, P., Cobbold, P., Reich, M., 2005. Mesozoic to Paleogene stratigraphy of the Atacama (Purilactis) Basin, Antofagasta region, northen Chile: insight into the earlier stages of central Andean tectonic evolution. Tectonophysics 399, 125–154.
Mpodozis, C., Ramos, V.A., 2008. Tectónica jurásica en Argentina y Chile: Extensión, Subducción Oblicua, Rifting Deriva y Colisiones? Rev. Geol. Argent. 63, 479–495.
Panien, M., Schreus, G., Pfiffner, A.O., 2005. Sandbox experiments on basin inversion: testing the influence of basin orientation and basin fill. J. Struct. Geol. 27, 433–445.
Peña, M., Arriagada, C., Martínez, F., Becerra, J., 2013. Carta Geológica Yerbas Buenas-Tres Morros, Región de Atacama. Servicio Nacional de Geología y Minería, scale: 1:100.000.
Petford, N., Cruden, A.R., McCaffrey, K.J.W., Vigneresse, J.-L., 2000. Granite magma formation, transport and emplacement in the Earth's crust. Nature 408, 669–673.
Ramberg, H., 1981. Gravity, Deformation and the Earth's Crust in Theory, Experiments and Geologic Application, 2nd ed. Academic Press, London, pp. 452.
Ramos, V., 2009. Anatomy and global context of the Andes: main geologic features and the Andean orogenic cycle. Geol. Soc. Am. Mem. 204, 31–65.
Román-Berdiel, T., Gapais, D., Brun, J.-P., 1997. Granite intrusion along strike-slip zones in experiment and nature. Am. J. Sci. 297, 651–678.
Román-Berdiel, T., 1999. Geometry of granite emplacement in the upper crust: contributions of analogue modelling. In: Castro, A., Fernandez, C., Vigneresse, J.L. (Eds.), Understanding Granites: Integrating New and Classical Techniques, vol. 168. Geological Society, Special Publication, London, pp. 77–94.
Román-Berdiel, T., Aranguren, A., Cuevas, J., Tubía, J.M., Gapais, D., Brun, J.P., 2000. Experiments on granite intrusions in transtension. In: Vigneresse, J.L., Mart, Y., Vendeville, B. (Eds.), Salt, Shale and Igneous Diapirs in and Around Europe, vol. 174. Geological Society, Special Publications, London, pp. 21–42.
Schellart, W.P., 2000. Shear test results for cohesion and friction coefficients for different granular materials: scaling implications for their usage in analogue modelling. Tectonophysics 324, 1–16, http://dx.doi.org/10.1016/S0040-1951(00)00111-6.
Schreurs, G., Buiter, S.J.H., Corti, G., Costa, E., Hoth, S., Koyi, H., Kukowski, N., Lohrmann, J., Schlische, R.W., Withjack, M.O., Boutelier, D., Cavozzi, C., Cruden, A., Daniel, J.-M., DelVentisette, C., Elder Brady, J.A., Hoffmann-Rothe, A., Mengus, J.-M., Montanari, D., Nilforoushan, F., Ravaglia, A., Yamada, Y., 2006. Analogue benchmarks of shortening and extension experiments. In: Buiter, S.J.H., Schreurs, G. (Eds.), Analogue and Numerical Modelling of Crustal-Scale Processes, vol. 253. Geological Society of London, Special Publications, pp. 1–27.
Sibson, R.H., 1995. Selective fault reactivation during basin inversion: potential for fluid redistribution through fault-valve action. In: Buchanan, J.G., Buchanan, P.G. (Eds.), Basin Inversion, vol. 88. Geological Society of London Special Publication, pp. 3–19.
Tibaldi, A., 2005. Volcanism in compressional tectonic settings: is it possible? Geophys. Res. Lett. 32, http://dx.doi.org/10.1029/2004GL021798.
Tibaldi, A., 2008. Contractional tectonics and magma paths in volcanoes. J. Volcanol. Geotherm. Res. 176, 291–301.
Tibaldi, A., Pasquaré, F., Tormey, D., 2010. Volcanism in reverse and strike-slip fault setting. In: Cloetingh, S., Negendank, J. (Eds.), New Frontiers in Integrated Solid Earth Sciences. International Year of Planet Earth., http://dx.doi.org/10.1007/978-90-481-2737-5.
Watanabe, T., Koyaguchi, T., Seno, T., 1999. Tectonic stress controls on ascent and emplacement of magmas. J. Volcanol. Geotherm. Res. 91, 65–78.
Weijermars, R., 1986. Flow behaviour and physical chemistry of bouncing putties and related polymers in view of tectonic laboratory applications. Tectonophysics 124, 325–358.